Petroleum Science 21 (2024) 3350–3362

Contents lists available at ScienceDirect

Petroleum Science

journal homepage: www.keaipublishing.com/en/journals/petroleum-science

Original Paper

Morphological complexity and azimuthal disorder of evolving pore space in low-maturity oil shale during in-situ thermal upgrading and impacts on permeability

Jun Liu [a, *], Yan-Bin Yao [b], Derek Elsworth [c]

[a] Key Laboratory of Deep Underground Science and Engineering (Ministry of Education), Institute of New Energy and Low-Carbon Technology, Sichuan University, Chengdu, 610065, Sichuan, China
[b] School of Energy Resource, China University of Geosciences Beijing, Beijing, 100083, China
[c] Department of Energy and Mineral Engineering, Pennsylvania State University, University Park, PA, 16802, USA

ARTICLE INFO

Article history:
Received 26 November 2023
Received in revised form
21 March 2024
Accepted 23 March 2024
Available online 28 March 2024

Edited by Yan-Hua Sun

Keywords:
Low-maturity oil shale
Fractal dimension
Form factor
Pore structure
Fluid seepage capacity

ABSTRACT

In-situ thermal upgrading is used to tune the pore system in low-maturity oil shales. We introduce fractal dimension (D), form factor (ff) and stochastic entropy (H) to quantify the heating-induced evolution of pore morphological complexity and azimuthal disorder and develop a model to estimate the impact on seepage capacity via permeability. Experiments are conducted under recreated in-situ temperatures and consider anisotropic properties—both parallel and perpendicular to bedding. Results indicate that azimuthal distribution of pores in the bedding-parallel direction are dispersed, while those in the bedding-perpendicular direction are concentrated. D values indicate that higher temperatures reduce the uniformity of the pore size distribution (PSD) in the bedding-parallel direction but narrow the PSD in the bedding-perpendicular direction. The greater ff (> 0.7) values in the bedding-parallel direction account for a large proportion, while the dominated in the bedding-perpendicular direction locates within 0.2–0.7, for all temperatures. The H value of the bedding-parallel sample remains stable at ~0.925 during heating, but gradually increases from 0.808 at 25 °C to 0.879 at 500 °C for the bedding-perpendicular sample. Congruent with a mechanistic model, the permeability at 500 °C is elevated ~1.83 times (bedding-parallel) and ~6.08 times (bedding-perpendicular) relative to that at 25 °C—confirming the effectiveness of thermal treatment in potentially enhancing production from low-maturity oil shales.

1. Introduction

The increasing energy demand and the resulting energy supply concerns become an important item on the agenda all over the world, which has deeply stimulated the commercial development of unconventional energy resources, as shale oil is one of such (Xu et al., 2022; Drouven et al., 2023; Lin et al., 2023; Wang et al., 2023a, b). The shale oil actually is the product of the thermal reaction and decomposition of kerogen present in oil shales (Han et al., 2015; Feng et al., 2020; Dang et al., 2022; Gou and Xu, 2023), containing far-reaching potential to increase the global oil supply for its huge reserve—as much as 6902 × 10^8 t (shale oil-equivalent reserves)—roughly three times the world's conventional crude oil reserve (Zhou et al., 2018). Although the shale oil exploitation has achieved sound performances, for example, it is aidant for American to become a net oil exporter (Vatter et al., 2022), the successful and effective extraction of shale oil is not easy, subjected to the complicated reservoir properties like pretty tight and high anisotropy (He et al., 2022; Syed et al., 2022; Bahadur et al., 2023; Bolotov et al., 2023; Wang et al., 2023a, b). In particular, the oil recovery from low-maturity oil shale keeps grand challenging because the oil there is not directly extractable, and thus additional techniques are required to make it producible (Feng et al., 2020; Yan et al., 2023).

Recent years, the heat treatment, aiming to ensure thermal upgrading, is placed great expectations, and is essentially a process that drives the in-situ pyrolysis of organic matter in low-maturity

* Corresponding author.
E-mail address: j.liu@scu.edu.cn (J. Liu).

https://doi.org/10.1016/j.petsci.2024.03.020

stage (Luo et al., 2021; Wang et al., 2021; Zhao et al., 2022; Zhang et al., 2023). Therein, once the heating is imposed, the inner pore system inevitably varies and this alteration is of significance, because it usually determines the storage capacity and seepage behavior of restoring oil (Wang et al., 2019; Li et al., 2020; Lei et al., 2021; Dang et al., 2022). Therefore, much attention has been devoted to the pore-related issue during in-situ upgrading of low-maturity oil shale. For instance, the pore structure evolution in oil shale (Liushuhe Basin, NE China) was investigated at variable high temperature treatments by mercury injection approach (Yang et al., 2016). And the heating-induced evolution of pore space in Permian oil shale from the Raniganj Basin (Eastern India) received a comprehensive description via joint methodologies, including FE-SEM, small-angle scattering, and CO_2—N_2 sorption (Chandra et al., 2023). In fact, there are many other similar attempts trying to emphasize the heating-induced alteration of pores in oil shale (Bai et al., 2017; Zhu et al., 2018; Huang et al., 2021; He et al., 2022; Wei and Sheng, 2022; Luo et al., 2023). Basically, current investigations on heating-induced pore variation are of guidance for the development of low-maturity oil shale to some degree.

However, that is not enough, at least supported by the limited commercial and effective oil extraction from low-maturity shale, which is, in fact, still awaiting more breakthroughs. As for the previous investigations on pore space variation by heating operation, they usually made the measurement when the oil shale sample is cooled from a certain elevated temperature (Bai et al., 2017; Huang et al., 2021; Chandra et al., 2023; Luo et al., 2023). In other words, sparing achievements are conducted by a federated scenario that the in-situ quantitative characterization of pore space alteration concurrently runs with the sustained heating on low-maturity oil shale. Therefore, this pore alteration issue still needs more responsible investigations like the real heating-induced variation of pore morphology and the resulting permeability change, which is of significance and thus drives this work to be arranged.

In this work, the real-time characterization of pore system is organized in the circumstance of elevated temperature enveloping the low-maturity oil shale, conducted by FE-SEM on a constant region during the gradual increase in temperature (up to 500 °C). Then SEM captures are digitized and translated into readable cross-sectional pore area (S), pore perimeter (C), and pore orientation (θ), depending on a machine learning method. Accordingly, the fractal dimension (D), the form factor (ff), and the stochastic entropy (H) are calculated, ensuring the quantitative and robust description on the morphology complexity and azimuth disorder of the evolving pore space in low-maturity oil shale by thermal upgrading. Simultaneously, their anisotropic characteristics are also involved, which is an intrinsic property of shale rock, but also is an easily overlooked point in previous heating-related pore studies. Besides, an estimation model of permeability is developed to assess the variation of seepage behavior—the inevitable consequence of pore space changes—for further investigating the evolving pore system during in-situ pyrolysis. Hopefully, this novel study brings a fresh perspective in in-situ alteration of pore space and seepage capacity when heating-up is applied to low-maturity oil shale.

2. Materials and methodology

2.1. Sample collection and preparation

The oil shale samples used in this work, with a buried depth of ~1080 m, are collected from the Songliao Basin, NE China (Fig. 1(a)). This shale core is from the Upper Cretaceous Qingshankou Formation that is recognized not just as a major source for conventional oil and gas, but also as a primary stratum for shale oil in the Songliao Basin (Jin et al., 2021; Lin et al., 2021; Wang et al., 2022). The shale sample herein presents a vitrinite reflectance of 0.92% (low-maturity) and a total organic carbon content of 4.4%. The collected core was cut and polished for the SEM observation, where the bedding-parallel and bedding-perpendicular samples are labeled as SH and SV, respectively, for the anisotropic investigation (Fig. 1(b)). The prepared samples have a length of ~4 mm, a width of ~3 mm, and a thickness of ~0.5 mm.

2.2. SEM image capture and digitization

This work presents the details of SEM setup for capturing real-time images and the related heating operation, and also expresses the basis logic for obtaining quantitative parameters from SEM images.

2.2.1. SEM image acquisition

The appearance of FE-SEM apparatus is exhibited in Fig. 2(a), where the SEM chamber is connected to an external water chiller for facilitating water circulation to control temperature during heating operation (Fig. 2(b)). Fig. 2(c) exhibits the interior scene of this apparatus, immersed in a high vacuum environment (i.e., 3×10^{-3} Pa) when SEM works. The temperature control wire is used to pass the temperature setting order, while the heat shield is set for keeping the fugitive emissions (electrons) off the detector and thus is helpful to improve the SEM imaging quality at elevated temperatures (Fig. 2(c)). The silicon heating substrate is responsible for heating the oil shale sample fastened by the screw/press clamp (Fig. 2(d)). Besides, a quality temperature sensor is mounted below the heating substrate to display the real-time temperature on the sample (Fig. 2(e)).

In this work, the working temperature begins from 25 °C, and then gradually increases to 100, 200, 300, 400, and 500 °C in sequence, with a rise rate of 5 °C/min for preventing the shale pore system from suffering any thermal shock (Fig. 3(a)). According to the previous experiences (Zhao et al., 2012; Luo et al., 2023; Liu et al., 2024), the exposure time of 2 h is set at each observation temperature to accommodate sufficient pyrolysis of the organic matter, followed by SEM capturing of the fixed view region. The selected fixed view for the bedding-parallel sample SH is presented in Fig. 3(b) with an area of ~1206 μm^2, while that for the bedding-perpendicular sample SV is measured as ~1732 μm^2 (Fig. 3(c)).

2.2.2. Quantitative parameter acquisition

The image processing with ImageJ from an SEM capture to quantitative parameters is roughly outlined in Fig. 4(a). The pixel-based machine learning is conducted using a trainable Weka segmentation plugin, learning what is pore and then discerning pore space from the acquired SEM scene. In this way, the pore information is calibrated and acquired, and more trainings are required if the former pore space recognition is dissatisfied, before the final pore system confirmation. Accordingly, the automatic measurement works, and the parameters are recorded, including pore area (S), pore perimeter (C), and pore orientation (θ). The detailed principle of machine learning using ImageJ can be reached in some previous works, like Arganda-Carreras et al. (2017), Lormand et al. (2018), and Thilagashanthi et al. (2021). By machine learning, the operation from the visual SEM capture to the digitized pore information is achieved—a digitization process in fact (Fig. 4(b)). As for the acquired parameters, C is defined as the summation length of boundary pixels, and S is determined by the pixel number in an enclosed pore (Fig. 4(c)). Simply, θ is treated as the rotation angle in clockwise for a certain pore to obtain its maximum Feret diameter which is interpreted in Sezer et al. (2008) and Liu et al. (2011), and it varies between 0° and 180°.

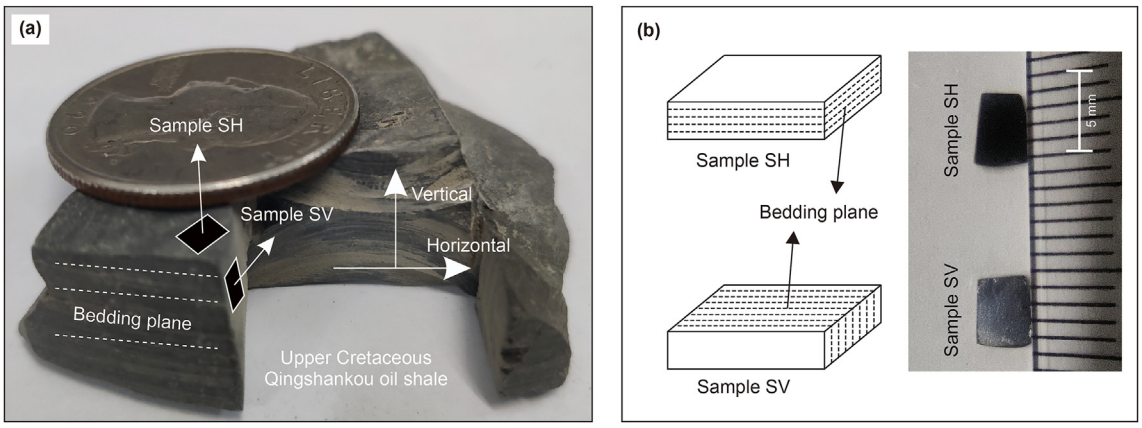

Fig. 1. Oil shale core involved in this work. (**a**) Core disc sample; (**b**) Preparation for FE-SEM.

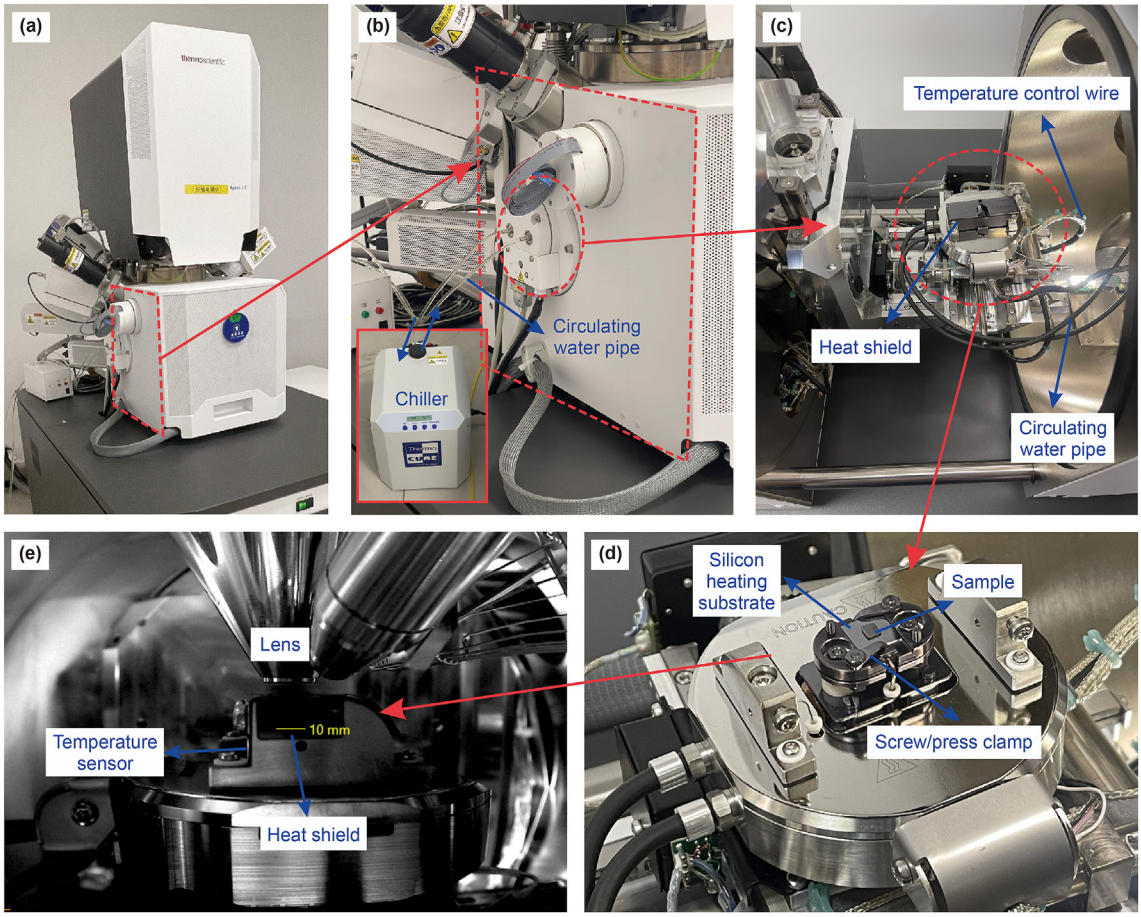

Fig. 2. FE-SEM setup with in-situ heated substrate. (**a**, **b**) Setup appearance; (**c**)–(**e**) Interior structure.

2.3. Theoretical support for quantitative data processing

On the basis of the acquired cross-sectional pore area (S), pore perimeter (C), and pore orientation (θ), the theoretical foundations for deriving fractal dimension (D) and form factor (ff)—for measuring pore morphology complexity, and stochastic entropy (H)—for evaluating pore azimuth disorder, are introduced; meanwhile, their significance in defining the pore space is also presented. We present the theoretical underpinnings of D, ff, and H in the following.

2.3.1. Fractal dimension (D)

Fractal dimension (D) presents a quantitative index for evaluating the uniformity of the pore size distribution (PSD) in porous rocks and is a relative mature approach (Dathe and Thullner, 2005; Yao et al., 2008; Liu et al., 2018; Wu et al., 2022). A variety of methodologies enable pore fractal property, such as low-field NMR approach (Zheng et al., 2018), low-temperature N_2 adsorption (Liu et al., 2018) and mercury intrusion porosimetry (Su et al., 2018), accompanied by corresponding theory foundation and calculation methods. In this work, the pore area (S) and pore perimeter (C)

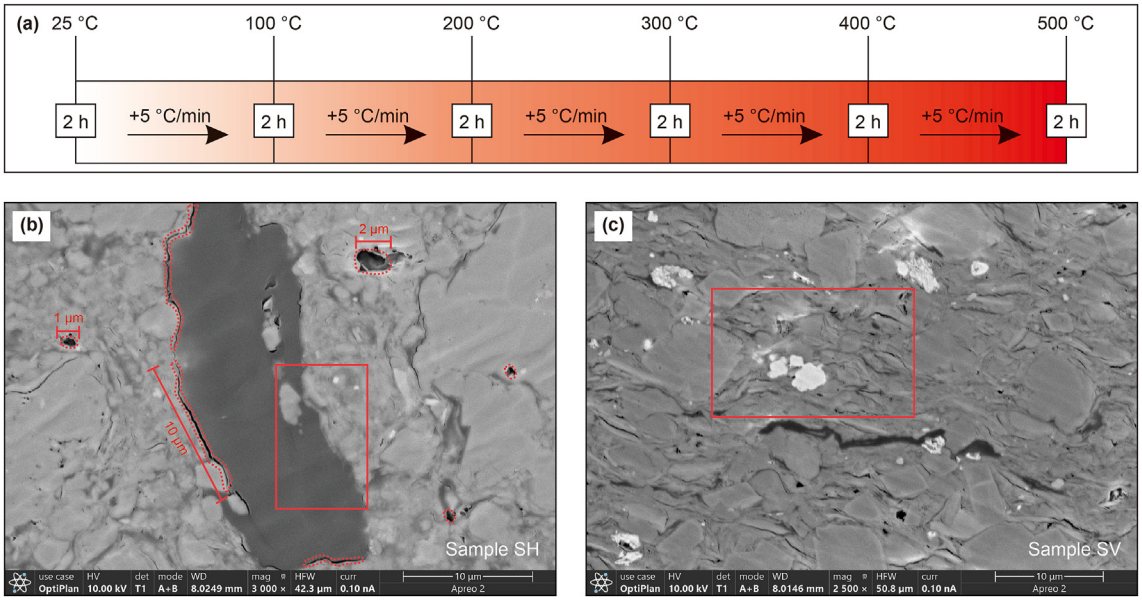

Fig. 3. Locations for temperature measurement and FE-SEM observation section. (**a**) Heating schedule; (**b, c**) Selected viewing/imaging windows for samples SH and SV, respectively.

originated from machine learning on SEM image, are applied for the acquisition of D values. For the pore system, D gives the rate of C change in response to the S change and the relationship among S, C, and D values follows this expression (Liu et al., 2011; Qi et al., 2014),

$$\log C = \frac{D}{2}\log S + c_1 \tag{1}$$

where a linear correlation goes to the log$C$–log$S$ plot on a log–log coordinates, in which the slope of this fitted line is $D/2$ and c_1 is the intercept (a constant). The D value varies in 1–2, and a greater D indicates a worse uniformity of the pore size distribution as well as a more complex pore microstructure.

2.3.2. Form factor (*ff*)

Form factor (*ff*) offers the description on the shape of pore features and reflects the rough edges of pore voids exhibited by the SEM image (Soroushian and Elzafraney, 2005; Cox and Budhu, 2008). It usually defined as

$$ff = \frac{4\pi S}{C^2} \tag{2}$$

where *ff* value is maximum at 1.0 for circles and 0.785 for squares, and a smaller *ff* value indicates a greater complexity of pore boundary, while it symbolizes an increasingly elongated shape as this value approaches 0.0.

By substituting Eq. (2) into Eq. (1), the expression is

$$\log ff = (1 - D)\log S - 2c_1 + \log 4\pi \tag{3}$$

Then, this equation is converted as

$$ff = 4\pi \times 10^{-2c_1} \times S^{1-D} \tag{4}$$

Simply,

$$ff = aS^{1-D} \tag{5}$$

where a equals $4\pi \times 10^{-2c_1}$. By this way, the relationship between form factor (*ff*) and fractal dimension (D) is built, that is, the D value indicates the *ff* variation along with the change of pore area (S), which follows a power function relationship.

2.3.3. Stochastic entropy (*H*)

Stochastic entropy (H) is a mathematical concept of probability and is a measure of the disorder, randomness, or uncertainty of a system. It serves far-ranging applications, such as in chemistry, economics and physics (Wehrl, 1978; Tietz et al., 2006). In geology field, stochastic entropy appears in a few works with respect to the investigations on soil and loess (Shi et al., 1996; Caniego et al., 2000; Wu et al., 2016; Liu et al., 2021), where the microstructure was evaluated with H values. In this work, the stochastic entropy is introduced as a measure of the pore directivity to characterize the disorder of azimuthal orientations of pore space in low-maturity oil shale, in a quantitative manner. Referring to the previous (Shi et al., 1996; Caniego et al., 2000), H is defined as

$$H = -\sum_{i=1}^{n} P_i \log_n P_i \tag{6}$$

where P_i indicates the percentage of pores in a particular azimuthal orientation. This work sets $i = 1$ to represent the 0°–10° orientation, then the whole azimuths (0°–180°) are equally divided into 18 segments, that is, $n = 18$ in this work. Basically, H value has a range from 0 to 1, and $H = 0$ means that all pores distribute in the same direction, while a greater H signals a stronger disorder in pore orientations, until $H = 1$—a totally stochastic distribution.

3. Results

Based on the SEM captures during heating, the variations of cross-sectional pore area (S), pore perimeter (C), and pore orientation (θ), as well as their anisotropic characteristics, along with the gradual rise of temperature are introduced.

3.1. Pore area (*S*)

As exhibited in Fig. 5, compared with the bedding-parallel sample SH, the bedding-perpendicular sample SV contains more

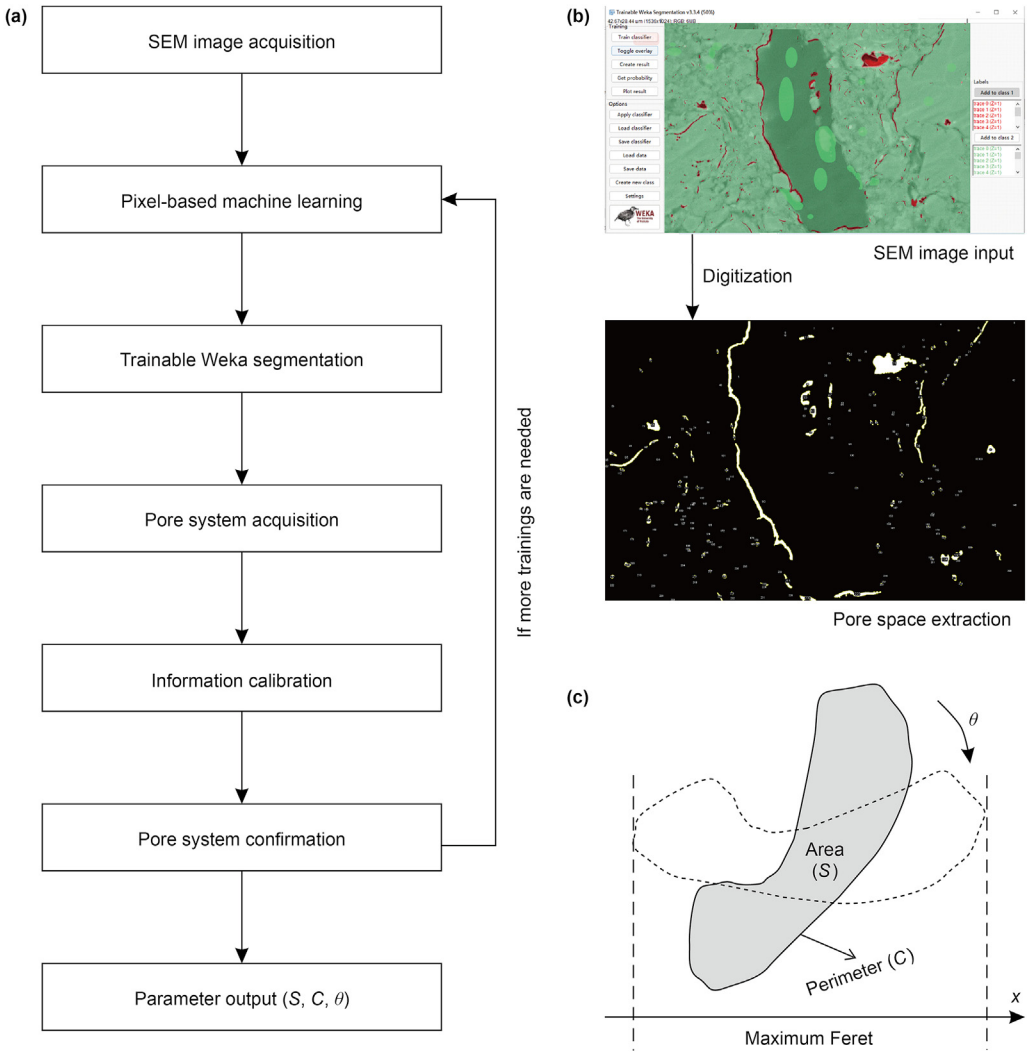

Fig. 4. Process of quantitative parameter acquisition. (**a**) Sketch for operation using trainable Weka segmentation; (**b**) Approximate description of the SEM image input and pore space extraction; (**c**) Schematic diagram defining pore parameters.

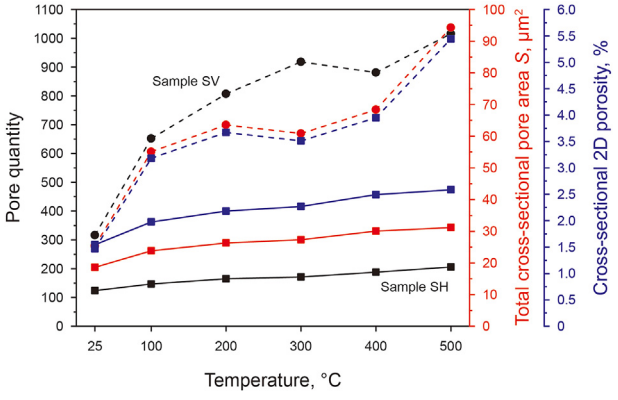

Fig. 5. Evolution of pore quantity and cross-sectional pore area with increased temperature. Dashed and solid lines represent samples SV and SH, respectively.

pores, greater cross-section pore area and superior 2D porosity at each temperature point, indicating the anisotropic property in pore structure. This phenomenon meets the previous works (Zhou et al., 2021, 2022). The anisotropy is also reflected in the different growth amplitude during heating operation. The sample SV experienced a greater increase amplitude in pore quantity, cross-section pore area and 2D porosity than the sample SH. For example, the total pore area becomes 31.18 μm^2 at 500 °C from 18.62 μm^2 at 25 °C for sample SH, while that increases to 94.26 μm^2 at 500 °C from 25.38 μm^2 at 25 °C for sample SV.

Basically, the pore quantity, pore area, and 2D porosity have an overall tendency to get greater along with rising temperature, but this growth tendency softly differs between samples SH and SV. As for the sample SH, this growth tends to be monotonical, and these statistical results from machine learning in Fig. 5 are directly revealed by the SEM exhibitions (Fig. 6)—more pores is generated at higher temperature, while, with respect to the sample SV, the growth trend fluctuates slightly. The heating operation for sample SV enables the general increase in pore quantity, indicated by the pore system comparison at variable temperature (Fig. 7), where, however, a mild decrease exists from 300 to 400 °C, resulted from some original unconnected pores get connected at higher temperature (illustrated by the area A in Fig. 7). Combining SEM observation with reasoning, this work suggests three principal factors influencing pore system during in-situ thermal upgrading of low-maturity oil shale, that is, (1) the organic matter pyrolysis

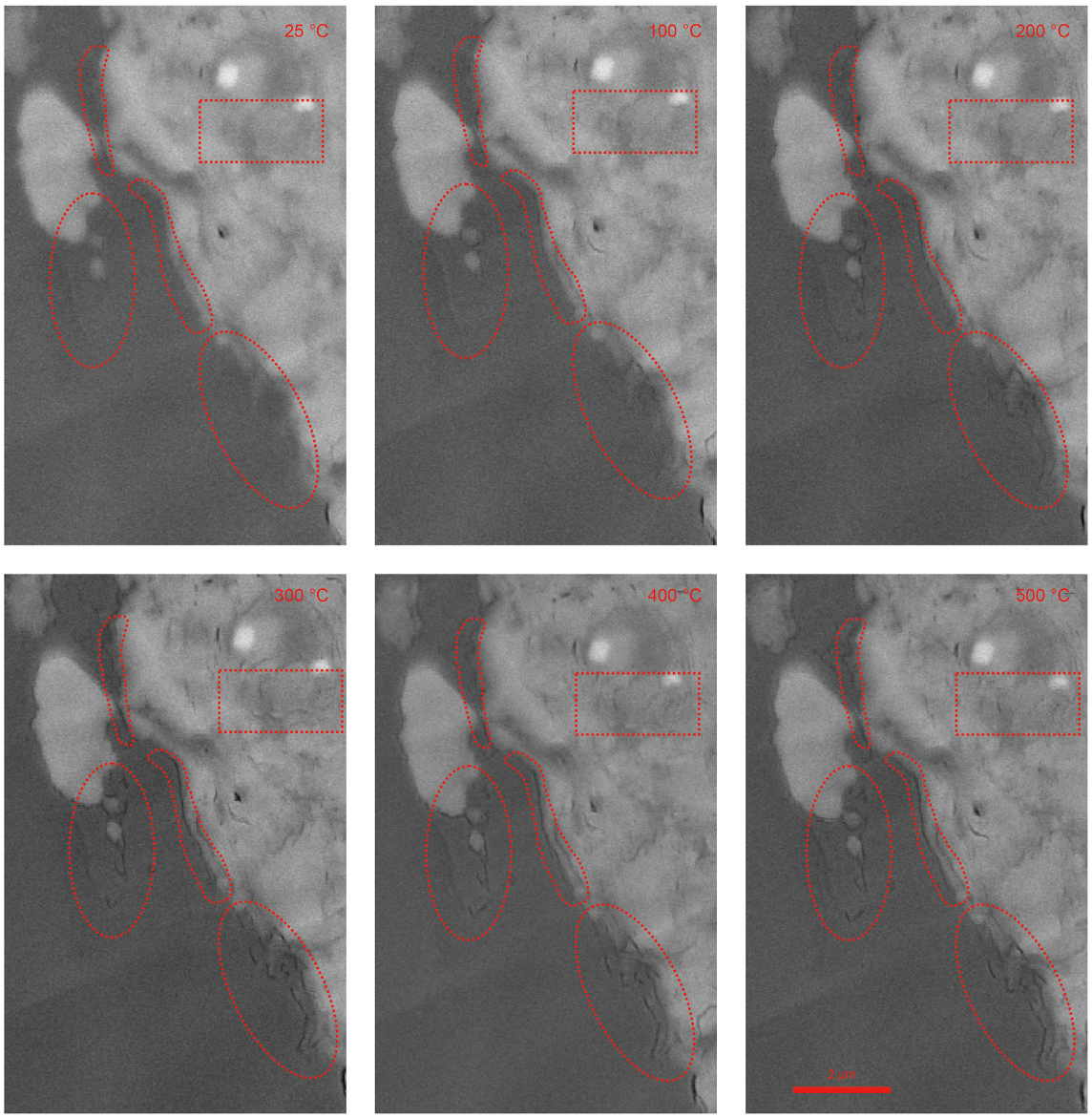

Fig. 6. SEM images during heating, showing pore system variation for sample SH. This representative region is shown as the rectangle in Fig. 3(b).

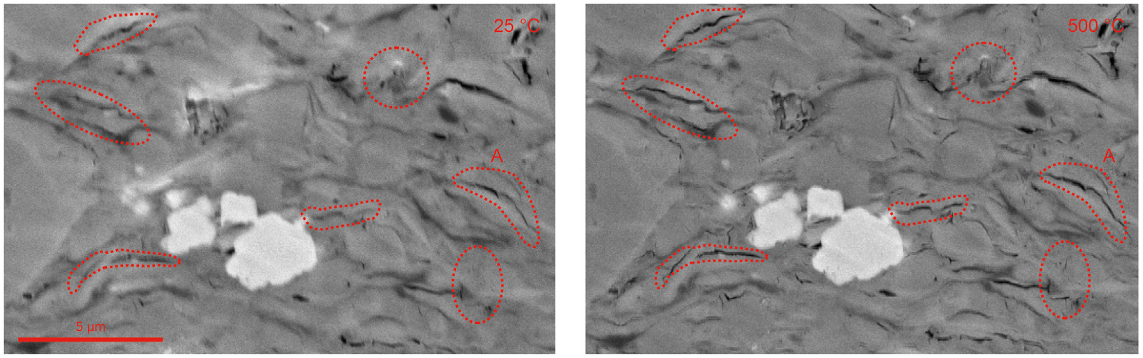

Fig. 7. SEM images at different temperatures for sample SV. This representative region is defined as the rectangle in Fig. 3(c).

develops new pore space and (2) heating-induced dehydration during illitization of clay minerals (He et al., 2022) shrinks the shale matrix, which enlarge the pore quantity and cross-sectional area, and (3) thermal expansion of shale matrix stimulated by elevated temperature—compressing pore space. However, the specific mechanism controlling the heating-induced variation of pore

system in low-maturity oil shale needs more specialized investigations.

3.2. Pore perimeter (C)

Increasing temperature ensures more pore quantity (Fig. 5) and thus enables the total pore perimeter to be enhanced (Fig. 8). Comparatively, the bedding-perpendicular sample SV has a superior total pore perimeter at each temperature point, accompanied with a greater increase amplitude at elevated temperature, than the bedding-parallel sample SH, indicating the existence of anisotropic phenomenon. The total perimeter is 247.87 μm at 25 °C and increases to 350 μm at 500 °C for sample SH (Fig. 8(a)), while it varies from 421.29 μm at 25 °C to 1550 μm at 500 °C for sample SV (Fig. 8(b)). The statistical chart in Fig. 8(a) indicates the newly-formed pores at elevated temperature tends to hold smaller perimeter than the original pores in sample SH, revealed by the narrower range for 10%–90% statistics, associated with an overall decrease of average and median values. This phenomenon suggests the newly-formed pores in the bedding-parallel direction seem to be smaller than the original ones, partly shown in Fig. 6. In addition, the statistics indicates the newly-formed pores in the bedding-perpendicular direction have a similar but fluctuant pore perimeter with the original ones for sample SV, illustrated by the 10%–90% statistics (Fig. 8(b)). Moreover, the connection of pores those are unconnected originally during heating, like the area A in Fig. 7, might be one reason for the fluctuant variation of pore perimeter.

3.3. Pore orientation (θ)

The orientation of pores in this work is not the geographic direction but a relative azimuth, in which the 90° for pores in sample SH is the direction towards the shale core center, while that in sample SV is the direction upwards and perpendicular to shale bedding. With respect to sample SH, the pore azimuths at each temperature condition show a multi-peak distribution, and the peaks differ at different temperature (Fig. 9(a)). For example, the pore azimuths peak at segments 2, 4, 7, 9, 11, 13, and 17 at 25 °C, while those peak at segments 3, 5, 7, 9, 12, and 17 at 300 °C. This issue suggests the dominated azimuths of pores vary because of heating operation in the bedding-parallel direction. However, an overall trend exists that the general orientation of newly-formed locates (but not strictly) within the orientation of original pores, revealed by that the pore azimuths stay low at segments 1, 10, and 18 for all heating conditions. By comparison, the pore azimuths in sample SV are straightforward, i.e, all operation conditions enable a similar distribution which peaks at segments 2, 13, 16, and 17, indicating the heating sparingly disturbs the pore azimuths (Fig. 9(a)). In other words, the orientation of newly-formed pores largely follows that of original ones during thermal upgrading of low-maturity oil shale in the bedding-perpendicular direction. The difference of variation tendency regarding pore azimuths in samples SH and SV suggests the anisotropic evolution of pore orientation in the bedding-parallel and bedding-perpendicular directions.

4. Discussion

According to the measured results, the values of fractal dimension (D) and form factor (ff) are calculated per Eqs. (1)–(5) for quantifying the pore morphology, while the values of stochastic entropy (H) from Eq. (6) are obtained to assess the pore azimuth disorder. Furthermore, this work develops a mathematical model of permeability and accordingly investigates the heating-induced variation on seepage capacity of low-maturity oil shale.

4.1. Complexity evolution of pore morphology

Based on the measurements of cross-sectional pore area (S) and pore perimeter (C), the log$S$–log$C$ plots for samples SH and SV under different temperatures are made (Fig. 10), where the linear correlations between log$S$ and log$C$ are strong—all R^2 values are greater than 0.93. Accordingly, based on Eq. (1), the D values are calculated and plotted in Fig. 11. For two samples, the D value varies at different temperatures, indicating the uniformity of pore microstructure changes under elevated temperature. At 25 °C, the initial D of sample SH ($D = 1.4172$) is greater than that of sample SV ($D = 1.3454$), suggesting a relatively worse uniformity of the original pore size distribution (before heating) in the bedding-parallel direction than in the bedding-perpendicular direction; however, this law experiences a reversal during heating operation—elevated temperature enables the D values of sample SH to become inferior relative to that of sample SV (Fig. 11). Meanwhile, the D variation tendency differs for two samples, where the D value tends to decrease at < 400 °C and then increase at > 400 °C for sample SH, while that increases first (< 400 °C), and then decreases (> 400 °C) for sample SV. This suggests the overall pore complexity has an opposite change law in the bedding-parallel and bedding-perpendicular directions. This phenomenon is treated as a newfound information and its specific mechanism requires more

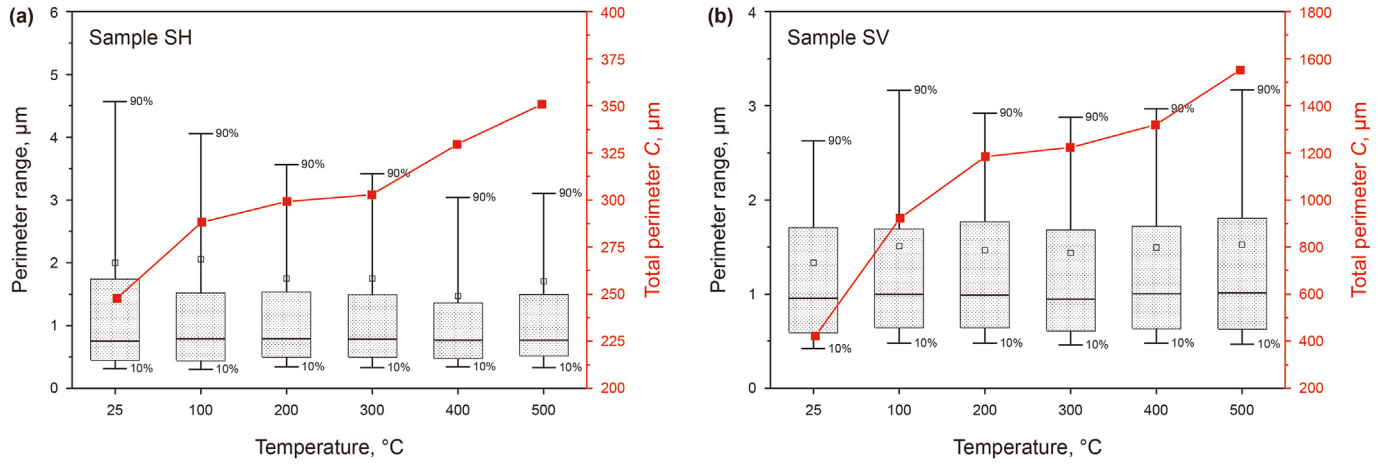

Fig. 8. Pore perimeter variation during heating operation. (**a**) Sample SH; (**b**) Sample SV.

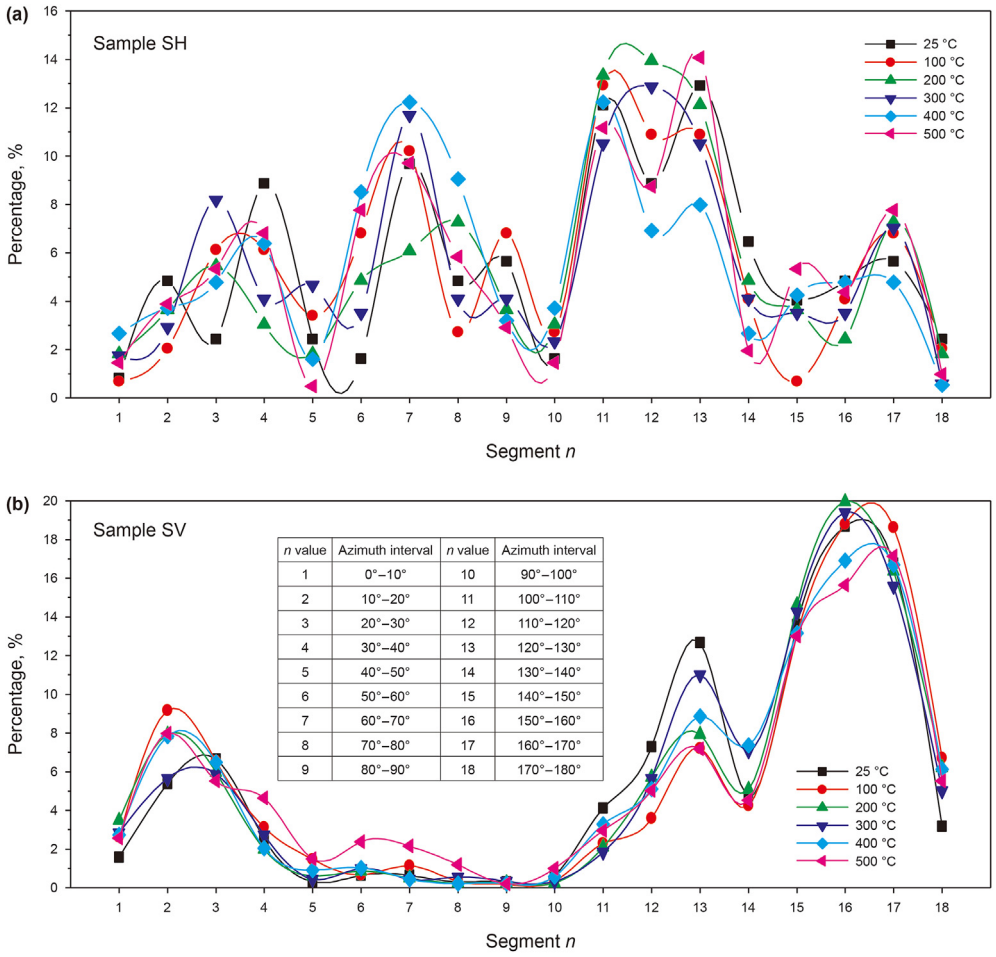

Fig. 9. Pore orientation at different azimuthal intervals at various temperatures. (**a**) Sample SH; (**b**) Sample SV.

attentions and detailed investigations.

Per Eq. (2), the form factor (*ff*) for each individual pore is obtained, and the statistics of all *ff* values are displayed in Fig. 12. As for the sample SH, Fig. 12(a) indicates that the percentage of different *ff* values differs, and there is an overall trend (but not strict) that greater *ff* values seem to be predominant. By comparison, regarding the sample SV (Fig. 12(b)), the dominated *ff* values locate within 0.2–0.7, which is suitable in all situations. Relatively, the different distribution of *ff* values suggests an anisotropic complexity of pore boundary, that is, the pores with stronger pore complexity in the bedding-perpendicular direction have a greater proportion than those in the bedding-parallel direction. In addition, it seems that the elevated temperature tends not to exaggeratively revise the original *ff* distribution at 25 °C, although slight fluctuations exist in the heating-induced alteration of *ff* values. This rule is appropriate for either sample, indicating that the newly-formed pores in low-maturity oil shale during pyrolysis follow the general complexity (*ff* value) of original pores (before heating).

Eq. (5) suggests a power-like function relationship between *ff* and *S* values, and this is validated in Fig. 13 by taking the situations of sample SH at 100 °C and sample SV at 300 °C as examples. In Fig. 13(a), the index of the power function is −0.412 and approximates to 1−1.4056 (1.4056 is the *D* value of sample SH at 100 °C, Fig. 11); and the similar cognition goes to Fig. 13(b) about the sample SV at 300 °C, following Eq. (5). As a result, the *D* value actually presents the *ff* value alteration when the *S* value increases. In extreme case, when $D = 1$, *ff* becomes a constant ($4\pi \times 10^{-2c_1}$) based on Eq. (5), while the situation of $D = 2$ enables the pore boundaries to present a 2D feature, because of the same index for *S* and *C* in Eq. (1) ($\log C = \log S + c_1$). Fig. 13 also indicates that for smaller pores ($S < \sim 1\ \mu m^2$), the decline rate of *ff* value rises with smaller *D* value, along with the increase in *S* value, suggesting the dramatic augment of pore boundary complexity in this process. On the contrary, for bigger pores ($S > \sim 1\ \mu m^2$), when the *S* value increases, the decline rate of *ff* value increases with greater *D* value. This comparison indicates a different law for pores with diverse size (demarcation size of ~1 μm^2) with respect to the relations among *D*, *S*, and *ff* values.

4.2. Response of pore azimuthal disorder

Depending on the pore orientation measurements (Fig. 9), the stochastic entropy (*H*) is calculated per Eq. (6), with the intention of determining the azimuth disorder of pores in low-maturity oil shale and its variation under elevated temperature (Fig. 14). Basically, the sample SH exhibits greater *H* values than the sample SV at all temperature settings, signaling a stronger disorder in pore orientations in the bedding-parallel direction, compared to the bedding-perpendicular direction. This phenomenon is in accord with the relatively more centralized distribution of the pore orientation in the sample SV, as shown by Fig. 9. With respect to the sample SH, the heating operation seems to barely disrupt the *H* values those are all around ~0.925 with a standard deviation of only 0.0096. Comparatively, for the sample SV, the *H* value is 0.808 at

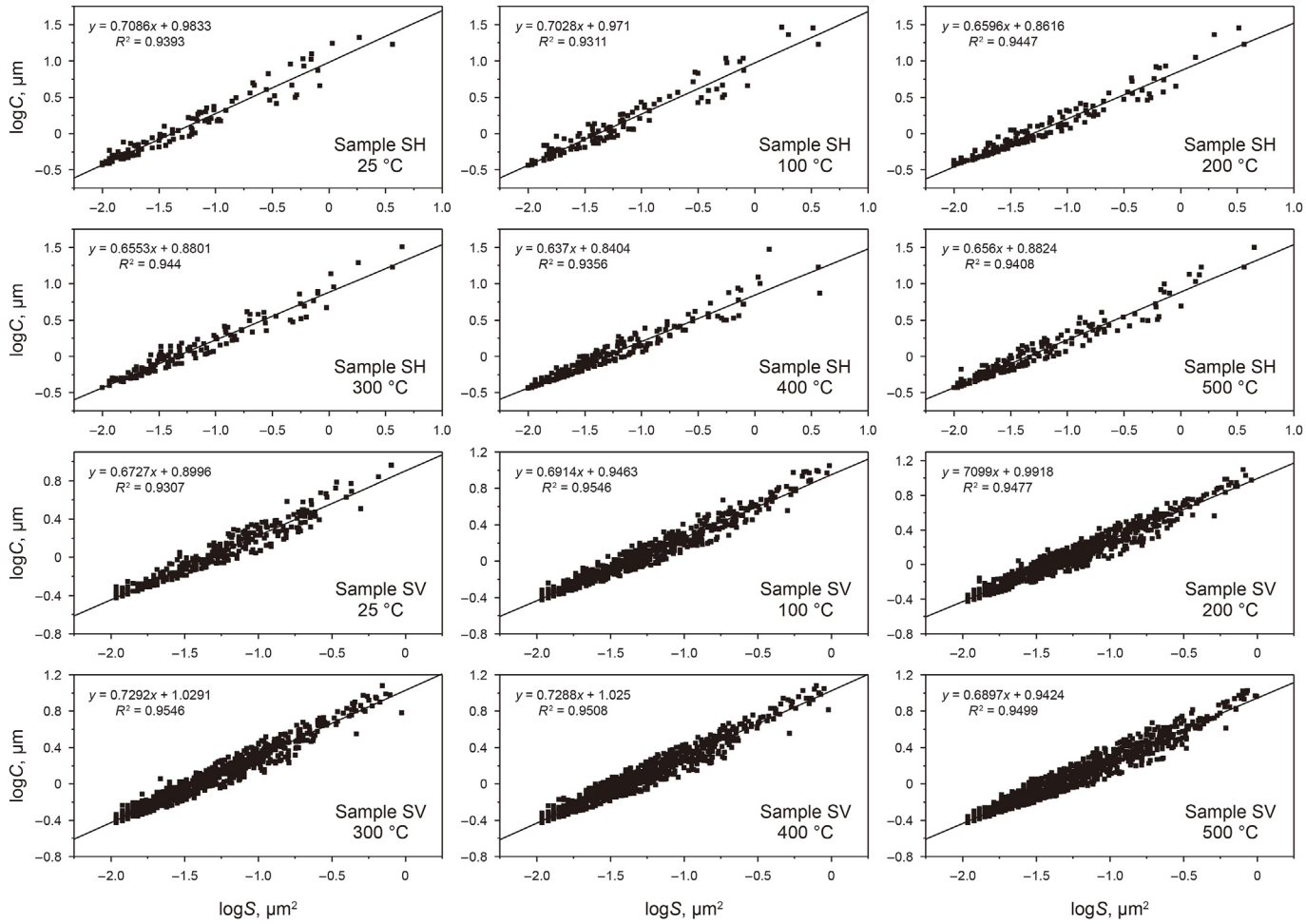

Fig. 10. Variation in log$S$ vs. log$C$ defining fractal dimensions of pore structures in the low-maturity oil shale.

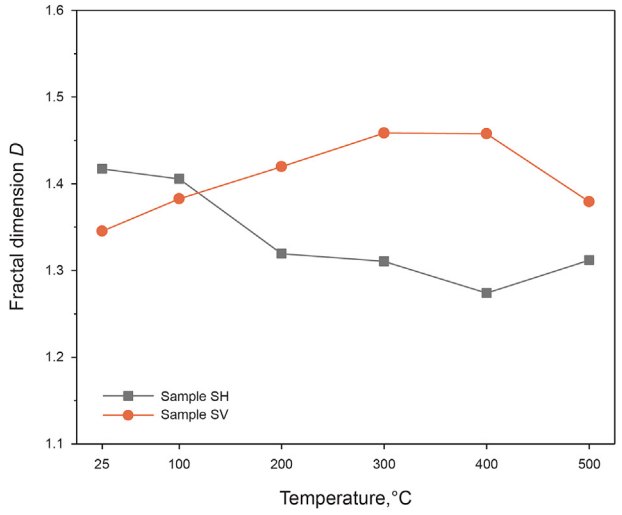

Fig. 11. Variation in fractal dimension (D) with temperature.

25 °C, gradually increases with rising temperature, and finally gets 0.879 at 500 °C. In summary, in the bedding-parallel direction, the stimulated pores during thermal upgrading follow the initial degree of pore azimuth disorder before heating, and thus the pyrolysis behavior scarcely enhances or dwindles the azimuth disorder of pores. However, in the bedding-perpendicular direction, the elevated temperature tends to boost the H value, and a higher temperature usually corresponds to a greater H value, indicating the stronger disorder of pore azimuth exists in the pores induced by higher temperature than those provoked by relatively lower temperature.

4.3. Seepage behavior of pore system

Seepage capacity influenced by heating is of significance for low-maturity oil shale, since it is the key factor determining fluids flow during/after in-situ thermal upgrading. This work firstly develops an estimation model for the seepage capacity evaluation, depending on the parameters acquired from SEM images, and then accordingly displays the alteration of seepage capacity under elevated temperature.

4.3.1. Calculation model development

In this work, the seepage capacity of the evolving pore space is estimated by the permeability. On the basis of Ergun–Wu equation (Wu et al., 2008), Wu et al. (2022) deduced the permeability (k) of porous media,

$$k = \frac{D_P^2 \phi^3}{72\tau(1-\phi)^2} \tag{7}$$

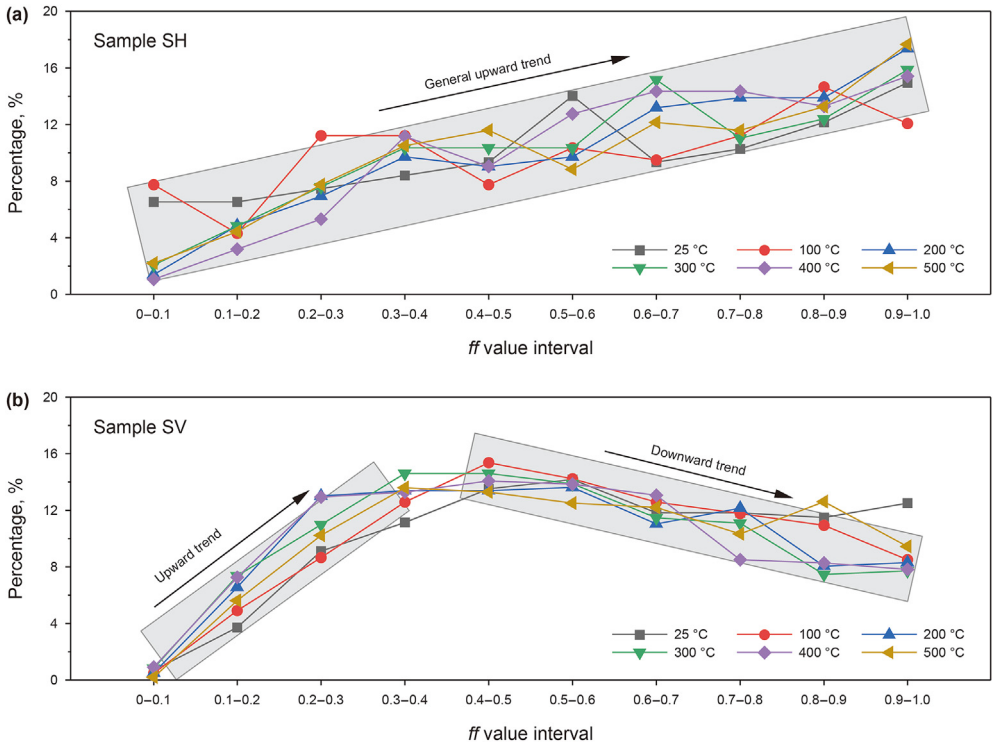

Fig. 12. Percentages representing form factors over different intervals under elevated temperatures. (**a**) Sample SH; (**b**) Sample SV.

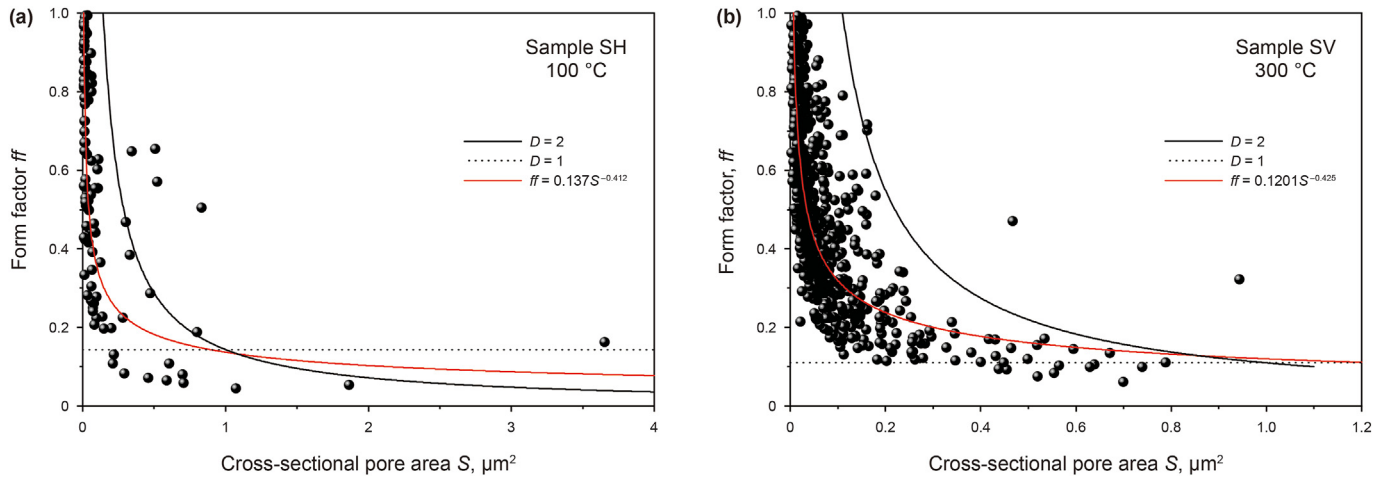

Fig. 13. Relationship between form factor and pore area. (**a**) Sample SH; (**b**) Sample SV. Red lines are the fitted using a power function.

where D_P is the average diameter of capillaries; ϕ is the porosity; τ is the tortuosity.

To acquire the permeability, this work bestows a small thickness to the 2D SEM image and thus imagines it as a 3D cube, as exhibited by Fig. 15(a). By this way, a 2D pore cross-section is regarded as a 3D column-like pore which has a τ of 1 (Fig. 15(b)). Therein, each individual capillary is straight and thus has a $\tau = 1$. Besides, the D_P has a correlation with the average hydraulic radius (R_h) (Wu and Yu, 2007),

$$D_P = \frac{6R_h(1-\phi)}{\phi} \tag{8}$$

where R_h is able to obtained by the area (S) and the perimeter (C) of the pore—the cross-sectional form of a certain irregular capillary, that is,

$$R_h = \frac{S}{C} \tag{9}$$

In addition, for an individual capillary, its porosity (ϕ) is

$$\phi = \frac{S_i}{S_w} \times 100\% \tag{10}$$

where S_i is the cross-sectional area of a certain pore in SEM image; S_w is the whole area of the selected fixed view of SEM image.

With the insertion of Eqs. (8)–(10) into Eq. (7), for a certain pore

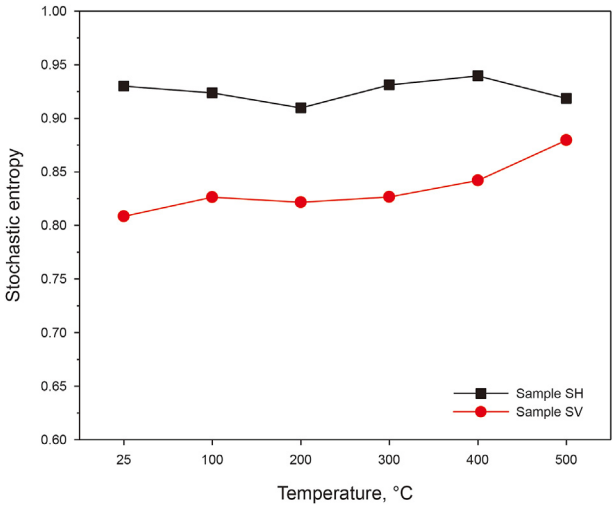

Fig. 14. Stochastic entropy at different pore azimuths and at different temperatures.

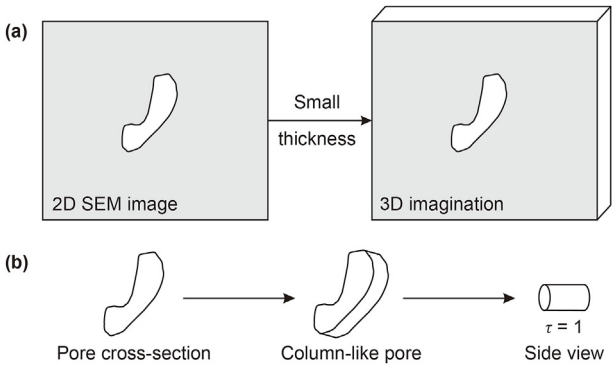

Fig. 15. Schematic diagram for imagining a 2D SEM image as a 3D form.

in SEM image, its individual seepage capacity (permeability k_i) yields

$$k_i = \frac{S_i^5}{8S_w^3 C_i^2} \tag{12}$$

where C_i is the perimeter of a certain pore.

With respect to the seepage capacity of the SEM image, it comprises the cumulative permeabilities of all pores within the scope of SEM capture. So, the seepage capacity (K) of the whole pores in the SEM image comes from

$$K = \sum_{i=1}^{N} k_i = \sum_{i=1}^{N} \frac{S_i^5}{8S_w^3 C_i^2} \tag{13}$$

where N is the detected pore number in the SEM image. The S_w value for samples SH and SV is ~1206 and ~1732 μm^2, respectively.

Per Eq. (13), the seepage capacity of an SEM image, represented by the permeability, can be estimated by the area of the SEM fixed view and the measured cross-sectional area and perimeter of individual pore. Accordingly, the calculated K values of the two samples under all temperature settings are plotted in Fig. 16.

4.3.2. Heating-induced change in seepage capacity

Because of the relatively large pores (size of 1 μm or bigger) in sample SH (Fig. 3(b)), the calculated K value is roughly two orders of magnitude greater than that of sample SV at each temperature point (Fig. 16). The general trend is that higher temperature ensures greater K value, i.e., a stronger seepage capacity, for either sample. The K value is 1.708 × 10^{-10} μm^2 for sample SH (0.440 × 10^{-12} μm^2 for sample SV) at 25 °C (before heating), and it gets 3.128 × 10^{-10} μm^2 for sample SH (2.678 × 10^{-12} μm^2 for sample SV) at 500 °C. In comparison, the K value at 500 °C is ~1.83 times and ~6.08 times greater than that at 25 °C for samples SH and SV, respectively. This issue suggests the elevated temperature seems to make a stronger improvement for the seepage capacity in the bedding-perpendicular direction than in the bedding-parallel direction. However, for two samples, the heating-induced K enhancement is nonlinear but is fluctuant, that is, the 400 °C downgrades the K value obtained at 300 °C for sample SH, while the 200 °C produces a decline of K value than 100 °C for sample SV. As for this phenomenon, possibly, one reason is that some pores (seepage channels) are compressed by the thermal expansion of shale matrix; however, the detailed mechanism that causes the evolution of seepage capacity of low-maturity oil shale under heating requires more insightful works.

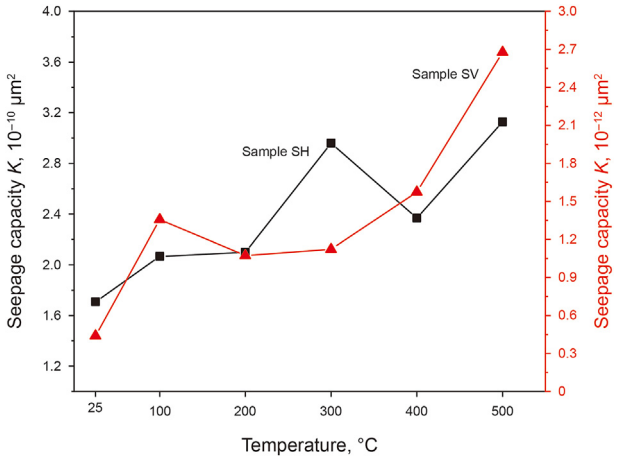

Fig. 16. Projected seepage capacity with temperature recovered from evolving pore geometry.

5. Conclusions

Two low-maturity oil shale samples are heated and simultaneously imaged by FE-SEM over a constant areal window. The acquired SEM images are digitized by machine learning to obtain fractal dimension, D, form factor, ff, and stochastic entropy, H, to characterize and describe the evolving morphological complexity and azimuthal disorder of the pore structure during thermal upgrading. Furthermore, these observed changes in pore structure are used to project anticipated seepage behavior through a pore-scale capillary model. The main conclusions yielded are as follows.

Elevated temperature increases both the number of pores and pore cross-sectional area (i.e., 2D porosity) of individual pores—with greater amplification in the bedding-perpendicular direction relative to bedding-parallel. Comparatively, the heating-induced pores in the bedding-parallel direction tend to be smaller than the original pores. During thermal upgrading, the pore azimuths of newly-formed pores overall follow that of the original pores (before heating) with the PSD in the bedding-parallel direction more dispersed than those in the bedding-perpendicular direction.

Evolving fractal dimensions (D) indicate that higher temperatures reduce uniformity of the pore size distribution in the bedding-parallel direction, but increase uniformity in the bedding-

perpendicular direction. In the bedding-parallel direction, the *ff* values which are over 0.7 tend to be the primary during heating, while the dominated *ff* values locate within 0.2–0.7 in the bedding-perpendicular direction, being suitable in all temperature situations. Besides, the *D* value presents the *ff* value alteration when the *S* value increase, with a power-like function relationship.

For the bedding parallel sample (horizontal: SH), the specific entropies (*H*) remain constant at ~0.925 over the temperature range 25–500 °C. Bedding perpendicular sample (vertical: SV), the *H* values evolve from 0.808 at 25 °C to 0.879 at 500 °C. This indicates that the heating-induced pores follow the initial degree of pore azimuth disorder (before heating) in the bedding-parallel direction, while stronger disorder is resulted from the pores induced at higher temperatures for the bedding-perpendicular direction.

A capillary model scaling seepage capacity, as related to the permeability, *K*, is developed from the pore-scale attributes recovered from a fixed SEM window—the principal parameters being measured cross-sectional area and the perimeter of individual pore. Elevated temperatures enhance the seepage capacity (increase permeability) of this low-maturity oil shale, where permeability (*K*) at 500 °C are ~1.83 times (bedding-parallel: SH) and ~6.08 times (bedding-perpendicular: SV) greater than that at 25 °C. This observed increase in bedding-perpendicular permeability suggests that gravity drainage towards the bedding will be significantly enhanced allowing the intrinsically larger bedding-plane permeability to then effectively transport the gravity draining product. This represents an effective mechanism of permeability enhancement and improved recovery in such materials.

Data availability

Data will be made available on request.

CRediT authorship contribution statement

Jun Liu: Writing – original draft, Software, Methodology, Funding acquisition, Data curation, Conceptualization. **Yan-Bin Yao:** Writing – review & editing, Visualization. **Derek Elsworth:** Writing – review & editing.

Declaration of competing interest

The authors declare that the research was conducted in the absence of any commercial or financial relationships that could be construed as a potential conflict of interest.

Acknowledgements

This study was financially supported by the National Key Research and Development Program of China (Grant No. 2022YFE0129800) and the National Natural Science Foundation of China (Grant No. 42202204). Derek Elsworth acknowledges support from the G. Albert Shoemaker endowment.

References

Arganda-Carreras, I., Kaynig, V., Rueden, C., Eliceiri, K.W., Schindelin, J., Cardona, A., Sebastian Seung, H., 2017. Trainable Weka Segmentation: a machine learning tool for microscopy pixel classification. Bioimage informatics 33, 2424–2426. https://doi.org/10.1093/bioinformatics/btx180.

Bahadur, J., Chandra, D., Das, A., Vishal, V., Agrawal, A.K., Sen, D., 2023. Pore anisotropy in shale and its dependence on thermal maturity and organic carbon content: a scanning SAXS study. Int. J. Coal Geol. 273. https://doi.org/10.1016/j.coal.2023.104268.

Bai, F.T., Sun, Y.H., Liu, Y.M., Guo, M.Y., 2017. Evaluation of the porous structure of Huadian oil shale during pyrolysis using multiple approaches. Fuel 187, 1–8. https://doi.org/10.1016/j.fuel.2016.09.012.

Bolotov, A.V., Yuan, C.D., Varfolomeev, M.A., Taura, U.H., Al-Wahaibi, Y.M., Minkhanov, I.F., Derevyanko, V.K., Al-Bahry, S., Joshi, S., Tazeev, A.R., Kadyrov, R.I., Emelianov, D.A., Pu, W.F., Naabi, A., Hasani, M., Al Busaidi, R.S., 2023. In-situ combustion technique for developing fractured low permeable oil shale: Experimental evidence for synthetic oil generation and successful propagation of combustion front. Fuel 344, 127995. https://doi.org/10.1016/j.fuel.2023.127995.

Caniego, F.J., Martín, M.A., San José, F., 2000. Singularity features of pore-size soil distribution: Singularity strength analysis and entropy spectrum. Fractals 9, 305–316. https://doi.org/10.1142/S0218348X0100066X.

Chandra, D., Bakshi, T., Bahadur, J., Hazra, B., Vishal, V., Kumar, S., Sen, D., Singh, T.N., 2023. Pore morphology in thermally-treated shales and its implication on CO_2 storage applications: a gas sorption, SEM, and small-angle scattering study. Fuel 331, 125877. https://doi.org/10.1016/j.fuel.2022.125877.

Cox, M.R., Budhu, M., 2008. A practical approach to grain shape quantification. Eng. Geol. 96, 1–16. https://doi.org/10.1016/j.enggeo.2007.05.005.

Dang, W., Nie, H.K., Zhang, J.C., Tang, X., Jiang, S., Wei, X.L., Liu, Y., Wang, F.Q., Li, P., Chen, Z.P., 2022. Pore-scale mechanisms and characterization of light oil storage in shale nanopores: new method and insights. Geosci. Front. 13, 101424. https://doi.org/10.1016/j.gsf.2022.101424.

Dathe, A., Thullner, M., 2005. The relationship between fractal properties of solid matrix and pore space in porous media. Geoderma 129, 279–290. https://doi.org/10.1016/j.geoderma.2005.01.003.

Drouven, M.G., Cafaro, D.C., Grossmann, I.E., 2023. Mathematical programming models for shale oil & gas development: a review and perspective. Comput. Chem. Eng. 177, 108317. https://doi.org/10.1016/j.compchemeng.2023.108317.

Feng, Q.H., Xu, S.Q., Xing, X.D., Zhang, W., Wang, S., 2020. Advances and challenges in shale oil development: a critical review. Advances in Geo-Energy Research 4, 406–418. https://doi.org/10.46690/ager.2020.04.06.

Gou, Q.Y., Xu, S., 2023. The controls of laminae on lacustrine shale oil content in China: a review from generation, retention, and storage. Energies 16, 1987. https://doi.org/10.3390/en16041987.

Han, X., Liu, Q., Jiang, X., 2015. Heat transfer characteristic of oil shale particle during the retorting. Int. J. Heat Mass Tran. 84, 578–583. https://doi.org/10.1016/j.ijheatmasstransfer.2015.01.058.

He, W.Y., Meng, Q.A., Lin, T.F., Wang, R., Liu, X., Ma, S.M., Li, X., Yang, F., Sun, G.X., 2022. Evolution features of in-situ permeability of low-maturity shale with the increasing temperature, Cretaceous Nenjiang Formation, northern Songliao Basin, NE China. Petrol. Explor. Dev. 49, 516–529. https://doi.org/10.1016/S1876-3804(22)60043-0.

Huang, X.D., Yang, D., Kang, Z.Q., 2021. Three-phase segmentation method for organic matter recognition in source rocks via CT images: a case study on oil shale pyrolyzed by steam. Energy & Fuels 35, 10075–10085. https://doi.org/10.1021/acs.energyfuels.1c00917.

Jin, Z.J., Zhu, R.K., Liang, X.P., Shen, Y.Q., 2021. Several issues worthy of attention in current lacustrine shale oil exploration and development. Petrol. Explor. Dev. 48, 1471–1484. https://doi.org/10.1016/S1876-3804(21)60303-8.

Lei, J., Pan, B.Z., Guo, Y.H., Fan, Y.F., Xue, L.F., Deng, S.H., Zhang, L.H., Ruhan, A., 2021. A comprehensive analysis of the pyrolysis effects on oil shale pore structures at multiscale using different measurement methods. Energy 227, 120359. https://doi.org/10.1016/j.energy.2021.120359.

Li, Z.L., Duan, Y.G., Peng, Y., Wei, M.Q., Wang, R., 2020. A laboratory study of microcracks variations in shale induced by temperature change. Fuel 280, 118636. https://doi.org/10.1016/j.fuel.2020.118636.

Lin, M.R., Xi, K.L., Cao, Y.C., Zhu, R.K., Niu, X.B., Xin, H.G., Ma, W.J., 2023. Cyclicity related to solar activity in lacustrine organic-rich shales and their significance to shale-oil reservoir formation. Geosci. Front. 14, 101586. https://doi.org/10.1016/j.gsf.2023.101586.

Lin, T., Liu, X., Zhang, J., Bai, Y., Liu, J., Zhang, Y., Zhao, Y., Cheng, X., Lv, J., Yang, H., 2021. Characterization of multi-component and multi-phase fluids in the Upper Cretaceous oil shale from the Songliao Basin (NE China) using T_1–T_2 NMR correlation maps. Petrol. Sci. Technol. 39, 1060–1070. https://doi.org/10.1080/10916466.2021.1990318.

Liu, C., Shi, B., Zhou, J., Tang, C.S., 2011. Quantification and characterization of microporosity by image processing, geometric measurement and statistical methods: Application on SEM images of clay materials. Appl. Clay Sci. 54, 97–106. https://doi.org/10.1016/j.clay.2011.07.022.

Liu, F., Zhong, X., Liu, Z., Liang, S., Gao, Y., Wang, S., 2021. Experimental study on dynamic elastic modulus and damping ratio of undisturbed loess based on microstructure. J. Seismol. Res. 44, 105–112 (in Chinese with English abstract).

Liu, J., Yao, Y., Liu, D., Cai, Y., Cai, J., 2018. Comparison of pore fractal characteristics between marine and continental shales. Fractals 26, 1840016. https://doi.org/10.1142/s0218348x18400169.

Liu, J., Bai, X., Elsworth, D., 2024. Evolution of pore systems in low-maturity oil shales during thermal upgrading –Quantified by dynamic SEM and machine learning. Petrol. Sci. https://doi.org/10.1016/j.petsci.2023.1012.1021.

Lormand, C., Zellmer, G.F., Németh, K., Kilgour, G., Mead, S., Palmer, A.S., Sakamoto, N., Yurimoto, H., Moebis, A., 2018. Weka trainable segmentation plugin in ImageJ: a semi-automatic tool applied to crystal size distributions of microlites in volcanic rocks. Microsc. Microanal. 24, 667–675. https://doi.org/10.1017/S1431927618015428.

Luo, Q.Y., Zhang, L., Zhong, N.N., Wu, J., Goodarzi, F., Sanei, H., Skovsted, C.B., Suchy, V., Li, M.J., Ye, X.Z., Cao, W.X., Liu, A.J., Min, X., Pan, Y.Y., Yao, L.P., Wu, J., 2021. Thermal evolution behavior of the organic matter and a ray of light on the origin of vitrinite-like maceral in the Mesoproterozoic and Lower Cambrian

black shales: insights from artificial maturation. Int. J. Coal Geol. 244, 103813. https://doi.org/10.1016/j.coal.2021.103813.
Luo, Z.K., Lin, T.F., Liu, X., Ma, S.M., Li, X., Yang, F., He, B., Liu, J., Zhang, Y., Xie, L.Z., 2023. High-temperature-induced pore system evolution of immature shale with different total organic carbon contents. ACS Omega 8, 12773–12786. https://doi.org/10.1021/acsomega.2c07990.
Qi, J.F., Sui, W.H., Zhang, C.L., Xu, J.S., 2014. Calculation and analysis of the porosity and fractal dimension of red stratum sandstone based on SEM images processing. J. Eng. Geol. 22, 339–345 (In Chinese with English abstract).
Sezer, G.I., Kambiz, R., Bekir, K., Goktepe, A.B., Sezer, A., 2008. Image analysis of sulfate attack on hardened cement paste. Mater. Des. 29, 224–231. https://doi.org/10.1016/j.matdes.2006.12.006.
Shi, B., Wang, B.J., Jiang, H.T., 1996. Quantitative assessment of changes of microstructure for clayey soil in the process of compaction. Chin. J. Geotech. Eng. 18, 57–62 (In Chinese with English abstract).
Soroushian, P., Elzafraney, M., 2005. Morphological operations, planar mathematical formulations, and stereological interpretations for automated image analysis of concrete microstructure. Cement Concr. Compos. 27, 823–833. https://doi.org/10.1016/j.cemconcomp.2004.07.008.
Su, P.H., Xia, Z.H., Qu, L.C., Yu, W., Wang, P., Li, D.W., Kong, X.W., 2018. Fractal characteristics of low-permeability gas sandstones based on a new model for mercury intrusion porosimetry. J. Nat. Gas Sci. Eng. 60, 246–255. https://doi.org/10.1016/j.jngse.2018.10.008.
Syed, F.I., Dahaghi, A.K., Muther, T., 2022. Laboratory to field scale assessment for EOR applicability in tight oil reservoirs. Petrol. Sci. 19, 2131–2149. https://doi.org/10.1016/j.petsci.2022.04.014.
Thilagashanthi, T., Gunasekaran, K., Satyanarayanan, K.S., Klemes, J.J., 2021. Microstructural pore analysis using SEM and ImageJ on the absorption of treated coconut shell aggregate. J. Clean. Prod. 324, 129217. https://doi.org/10.1016/j.jclepro.2021.129217.
Tietz, C., Schuler, S., Speck, T., Seifert, U., Wrachtrup, J., 2006. Measurement of stochastic entropy production. Phys. Rev. Lett. 97, 050602. https://doi.org/10.1103/PhysRevLett.97.050602.
Vatter, M.H., Van Vactor, S.A., Coburn, T.C., 2022. Price responsiveness of shale oil: a Bakken case study. Natural Resources Research 31, 713–734. https://doi.org/10.1007/s11053-021-09972-9.
Wang, G.Y., Yang, D., Kang, Z.Q., Zhao, J., Lv, Y.Q., 2019. Numerical investigation of the in situ oil shale pyrolysis process by superheated steam considering the anisotropy of the thermal, hydraulic, and mechanical characteristics of oil shale. Energy & Fuels 33, 12236–12250. https://doi.org/10.1021/acs.energyfuels.9b02883.
Wang, G.P., Jin, Z.J., Liu, G.X., Wang, R.Y., Zhao, G., Tang, X., Liu, K.Q., Zhang, Q., 2023a. Pore system of the multiple lithofacies reservoirs in unconventional lacustrine shale oil formation. Int. J. Coal Geol. 273, 104270. https://doi.org/10.1016/j.coal.2023.104270.
Wang, J., Xie, H.P., Matthai, S.K., Hu, J.J., Li, C.B., 2023b. The role of natural fracture activation in hydraulic fracturing for deep unconventional geo-energy reservoir stimulation. Petrol. Sci. 20, 2141–2164. https://doi.org/10.1016/j.petsci.2023.01.007.
Wang, X.N., Li, J.R., Jiang, W.Q., Zhang, H., Feng, Y.L., Yang, Z., 2022. Characteristics, current exploration practices, and prospects of continental shale oil in China. Advances in Geo-Energy Research 6, 454–459. https://doi.org/10.46690/ager.2022.06.02.
Wang, Z.J., Yao, J., Sun, H., Yan, X., Yang, Y.F., 2021. A multi-continuum model for simulating in-situ conversion process in low-medium maturity shale oil reservoir. Advances in Geo-Energy Research 5, 456–464. https://doi.org/10.46690/ager.2021.04.10.
Wehrl, A., 1978. General properties of entropy. Rev. Mod. Phys. 50, 221–260. https://doi.org/10.1103/RevModPhys.50.221.
Wei, Z.J., Sheng, J.J., 2022. Study of thermally-induced enhancement in nanopores, microcracks, porosity and permeability of rocks from different ultra-low permeability reservoirs. J. Petrol. Sci. Eng. 209, 109896. https://doi.org/10.1016/j.petrol.2021.109896.
Wu, J.S., Yu, B.M., 2007. A fractal resistance model for flow through porous media. Int. J. Heat Mass Tran. 50, 3925–3932. https://doi.org/10.1016/j.ijheatmasstransfer.2007.02.009.
Wu, J.S., Yu, B.M., Yun, M.J., 2008. A resistance model for flow through porous media. Transport Porous Media 71, 331–343. https://doi.org/10.1007/s11242-007-9129-0.
Wu, J.S., Zhang, C.Y., Yu, B.M., Yin, S.X., Xing, M., Chen, X.X., Lian, H.Q., Yi, S.H., 2022. Fractal characteristics of low-permeability sandstone reservoirs. Fractals 30, 2250075. https://doi.org/10.1142/S0218348x2250075x.
Wu, K., Ni, W., Liu, H., Yuan, Z., Zhu, Q., Shi, B., 2016. Research on the relationships between the strength properties of compacted loess and microstructure changes. Hydrogeol. Eng. Geol. 43, 62–69 (In Chinese with English abstract).
Xu, Y., Lun, Z.M., Pan, Z.J., Wang, H.T., Zhou, X., Zhao, C.P., Zhang, D.F., 2022. Occurrence space and state of shale oil: a review. J. Petrol. Sci. Eng. 211, 110183. https://doi.org/10.1016/j.petrol.2022.110183.
Yan, G., Xu, Y.H., Xu, W.L., Bai, B., Bai, Y., Fan, Y.P., Li, S.S., Zhong, M., Liu, Y., Xu, Z.Y., 2023. Shale oil resource evaluation with an improved understanding of free hydrocarbons: insights from three-step hydrocarbon thermal desorption. Geosci. Front. 14, 101677. https://doi.org/10.1016/j.gsf.2023.101677.
Yang, L.S., Yang, D., Zhao, J., Liu, Z.H., Kang, Z.Q., 2016. Changes of oil shale pore structure and permeability at different temperatures. Oil Shale 33, 101–110. https://doi.org/10.3176/oil.2016.2.01.
Yao, Y.B., Liu, D.M., Tang, D.Z., Tang, S.H., Huang, W.H., 2008. Fractal characterization of adsorption-pores of coals from North China: an investigation on CH_4 adsorption capacity of coals. Int. J. Coal Geol. 73, 27–42. https://doi.org/10.1016/j.coal.2007.07.003.
Zhang, Y., Feng, D., Wan, S., Wang, Z., Yu, R., Zhang, P., Zhang, X., Feng, Y., 2023. Enhancing performance in organic solid structures and heat transfer with single annealing process and variable rates. Int. J. Heat Mass Tran. 213, 124306. https://doi.org/10.1016/j.ijheatmasstransfer.2023.124306.
Zhao, J., Wang, L., Liu, S.M., Kang, Z.Q., Yang, D., Zhao, Y.S., 2022. Numerical simulation and thermo-hydro-mechanical coupling model of in situ mining of low-mature organic-rich shale by convection heating. Advances in Geo-Energy Research 6, 502–514. https://doi.org/10.46690/ager.2022.06.07.
Zhao, J., Yang, D., Kang, Z.Q., Feng, Z.C., 2012. A micro-CT study of changes in the internal structure of Daqing and Yan'an oil shales at high temperatures. Oil Shale 29, 357–367. https://doi.org/10.3176/oil.2012.4.06.
Zheng, S.J., Yao, Y.B., Liu, D.M., Cai, Y.D., Liu, Y., 2018. Characterizations of full-scale pore size distribution, porosity and permeability of coals: a novel methodology by nuclear magnetic resonance and fractal analysis theory. Int. J. Coal Geol. 196, 148–158. https://doi.org/10.1016/j.coal.2018.07.008.
Zhou, H., Zeng, S., Zhan, L., Xu, G., Qian, Y., 2018. Modelling and analysis of oil shale refinery process with the indirectly heated moving bed. Carbon Resources Conversion 1, 260–265. https://doi.org/10.1016/B978-0-444-64241-7.50240-8.
Zhou, J.P., Yang, K., Zhou, L., Jiang, Y.D., Xian, X.F., Zhang, C.P., Tian, S.F., Fan, M.L., Lu, Z.H., 2021. Microstructure and mechanical properties alterations in shale treated via CO_2/CO_2-water exposure. J. Petrol. Sci. Eng. 196, 108088. https://doi.org/10.1016/j.petrol.2020.108088.
Zhou, J.P., Tian, S.F., Xian, X.F., Zheng, Y., Yang, K., Liu, J.F., 2022. Comprehensive review of property alterations induced by CO_2-shale interaction: Implications for CO_2 sequestration in shale. Energy & Fuels 36, 8066–8080. https://doi.org/10.1021/acs.energyfuels.2c01542.
Zhu, J.Y., Yang, Z.Z., Li, X.G., Wang, N.L., Jia, M., 2018. Evaluation of different microwave heating parameters on the pore structure of oil shale samples. Energy Sci. Eng. 6, 797–809. https://doi.org/10.1002/ese3.253.